JOURNAL OF SPACECRAFT AND ROCKETS
Vol. 33, No. 3, May–June 1996

Computational Fluid Dynamics Validation Using Multiple Interferometric Views of a Hypersonic Flowfield

R. R. Boyce,* J. W. Morton,† and A. F. P. Houwing‡
Australian National University, Canberra ACT 0200, Australia
C. Mundt§
Deutsche Aerospace, Munich 8000, Germany
and
D. J. Bone¶
Commonwealth Scientific and Industrial Research Organization, Canberra ACT 2601, Australia

The validity of the computed three-dimensional perfect-gas inviscid density field of the shock layer about a blunt body in a hypersonic argon freestream has been investigated. Mach–Zehnder interferometry was used to generate interferograms of such a flowfield produced in the T3 free-piston shock tunnel. Two-dimensional phase maps (representing line-of-sight integrated density) were produced from the interferograms using a two-dimensional Fourier transform fringe analysis method. Theoretical maps, computed from the computational fluid dynamics solution, compare extremely well with experimental maps for each of seven different viewing angles used to generate interferograms. The multiple angles remove the ambiguity associated with comparing theoretical and experimental integrated quantities. Thus, confidence can be placed in the validity of the three-dimensional density computations.

Nomenclature

A/A^* = nozzle area ratio
a = speed of sound, ms^{-1}
ds = distance increment along optical line of sight, m
dx = distance increment along nozzle axis, m
h = enthalpy, $MJkg^{-1}$
h_{ad} = adiabatic enthalpy, $MJkg^{-1}$
h_w = model wall enthalpy, $MJkg^{-1}$
K = Gladstone–Dale coefficient, m^3kg^{-1}
M = Mach number
P = pressure, kPa, MPa
P_{pitot} = pitot pressure, kPa
Pr = Prandtl number
Re = Reynolds number
r = distance normal to body axis of symmetry, mm; recovery factor
T = temperature, K
t = time, s
t_{NT} = nozzle transit time, s
t_s = nozzle shock transit time, s
u, v, w = Cartesian coordinate system for line-of-sight integration, m
v = velocity, ms^{-1}
x = distance from nose along body axis of symmetry, mm; distance from nozzle throat, m
Δ = incremental change
δ^* = displacement thickness, m
θ = azimuthal angle between the plane normal to the optical axis and the plane defined by the nozzle and model axes of symmetry, deg
λ = wavelength, m
μ = viscosity coefficient, $kgm^{-1}s^{-1}$
ρ = density, kgm^{-3}
ϕ = optical phase shift, rad

Subscripts

ref = Eckert's reference quantities
∞ = freestream
0, stg = reservoir, stagnation

Introduction

INCREASING importance is being placed on the use of computational fluid dynamics (CFD) codes as engineering tools in the design of new spacecraft. Before these codes can be applied confidently, however, it is essential that the numerical methods and physical and chemical models employed by them be thoroughly validated. The final results that represent the combination of the various models and algorithms used in the codes must be extensively checked against experimental data.[1]

Previous experiments in free-piston shock-tunnel facilities have produced data on shock shape, surface heat transfer rates, and shock-layer temperatures, and these have been compared with CFD predictions.[2–5] In addition, for two-dimensional hypervelocity nitrogen flows over cylinders, it has been possible to make direct comparisons between the interferometrically measured and CFD-predicted density fields.[6,7] This is because the interferometrically produced phase data are the result of the integration of the refractive index (and, hence, the species densities via the Gladstone–Dale relation for a multicomponent gas[8]) along the line of sight. For a two-dimensional flow, the flow parameters are constant along that line of sight, and so phase contours in the interferograms correspond directly to refractive index contours in the flowfield. For complex three-dimensional flows, however, such direct comparisons are not possible because of the varying flow conditions along the line of sight. Instead, the reliability of the code to predict the correct density field needs to be tested indirectly. This can be achieved by performing numerical line-of-sight integration of the density data produced by the code to yield theoretical phase maps. These phase maps can then be compared with those produced by interferometry

Received March 9, 1994; revision received Aug. 7, 1995; accepted for publication Aug. 7, 1995.

*Research Student, Physics, Aerophysics, and Laser Diagnostics Research Laboratory, Department of Physics and Theoretical Physics. Student Member AIAA.
†Research Student, Physics, Aerophysics, and Laser Diagnostics Research Laboratory, Department of Physics and Theoretical Physics.
‡Senior Lecturer, Physics, Aerophysics, and Laser Diagnostics Research Laboratory, Department of Physics and Theoretical Physics. Member AIAA.
§Research Engineer, Military Aircraft Division; currently Research Engineer, ET4, BMW-Rolls Royce Aeroengines, 15827 Dahlewitz, Germany. Member AIAA.
¶Research Scientist, Division of Information Technology, Center for Spatial Information Systems.

experiments. This indirect method has certain shortcomings though, because a range of different total and species density distributions can produce identical phase maps, which introduces a certain degree of ambiguity into the CFD validation process.

To overcome this problem, experimental work has been undertaken to provide a database that will eventually be used for the tomographic reconstruction of three-dimensional density distributions in the shock layer around a hyperboloid at nonzero incidence in hypersonic and hypervelocity flows. The database consists of phase maps for seven different viewing angles of the same flow and can be used for CFD validation purposes without performing a tomographic reconstruction. This paper presents such validation work, comparing theoretical phase maps generated from the perfect-gas three-dimensional coupled Euler/second-order boundary-layer CFD code of Mundt[9] with the perfect-gas part of the experimental database. The experimental phase maps were produced from interferograms taken of a low-stagnation enthalpy hypersonic argon flow generated in the T3 free-piston shock tunnel of the Australian National University. The aim is to investigate the validity of the density computation by removing the ambiguity of the line-of-sight measurements by using multiple viewing angles. The suitability of the data for tomographic reconstruction can then be discussed.

CFD Method

The CFD method[9,10] couples the solutions of the Euler and the second-order boundary-layer equations, providing an efficient calculation of the viscous hypersonic flow in regions where boundary-layer theory is valid. The inviscid flow is solved using a split-matrix algorithm, with Runge–Kutta time stepping, to solve the Euler equations that are discretized using a third-order accurate upwind biased formula. The equations are then integrated in time using a three-step Runge–Kutta procedure. A bow-shock fitting approach is used, with the computational grid extending from the body surface to the shock and, therefore, time dependent. At the shock, the Rankine–Hugoniot equations are applied, determining the shock velocity (in the transient phase) and shock shape. The viscous part of the flow is solved using the second-order boundary-layer equations in a locally monoclinic coordinate system. Because of their parabolic behavior in space, these equations are solved with a finite difference space-marching method. Boundary conditions for the second-order theory are prescribed at the outer edge of the boundary layer, interpolated from the inviscid profiles from the solution of the Euler equations. This procedure accounts for the effects of entropy-layer swallowing. The coupling procedure, necessary for transferring information between the equation systems, is as follows.[10] An equivalent mass-source distribution is calculated from the boundary-layer solution and impressed on the Euler calculation as a boundary condition at the body, filling the region between the body and the displacement thickness with fluid. The resulting equivalent inviscid flow, after convergence, is again coupled to the boundary-layer method, after which the calculation is then ended.

Various versions of the code allow the shock layer to be treated as either a perfect-gas, equilibrium chemistry flow (by means of vectorized thermodynamic and transport property state surfaces for nitrogen or air[3]) or nonequilibrium chemistry flow[10] (nitrogen or air). A two-dimensional/axisymmetric version is used for 0-deg angle of attack, whereas a fully three-dimensional version is used for higher angles of attack. The current work makes use of the three-dimensional perfect-gas code adapted for argon flows.

The computational grid for the present work was designed around a least-squares fit to the blunt body (an axisymmetric hyperboloid) used in the experiments:

$$(x/491.318 + 1)^2 - (r/86.356)^2 = 1 \qquad (1)$$

The body is truncated at $x = 75$ mm and has a nose radius of 15.18 mm and an asymptotic half-angle of 9.97 deg. Given the 75-mm length here, no parts of the body would be shielded from a parallel freestream for angles of attack less than 19.46 deg. The divergence of the freestream in this work is approximately 2.4 deg (half-angle) at the model base, and so angles of attack of less than 17 deg would not produce regions of the body that are shielded from the freestream. The angle of attack in the present case is 15 deg, representing a flow situation in which the application of the coupled Euler/boundary-layer method is valid. The surface mesh defining the body contained 38 points in the streamwise direction and 33 points in the crossflow direction (one side of the body only, making use of the body plane of symmetry). The grid was concentrated toward the stagnation region. For the inviscid shock layer, 17 points between the shock and the body surface were used; whereas for the boundary-layer calculation, 51 points between the boundary layer outer edge and the body surface were used. In both cases, the grid was concentrated toward the surface. An inviscid calculation using double the grid density in the streamwise and wall-normal directions was performed to check grid sensitivity. This yielded maximum deviations of the flow parameters from the coarse grid case of 2%. The sensitivity of the boundary-layer solution was not checked, but is not expected to be significant because at the flow conditions of interest here, the boundary-layer displacement effect was found to be negligible and the boundary-layer thickness for the front part of the body (where the experimental results are obtained) was only of the order of 5% of the shock-layer thickness.

Experiment

Flowfield

The experiments reported were performed on the Australian National University's T3 free-piston shock tunnel[11] (see Fig. 1). The tunnel is operated in reflected mode that produces variable pulsed high-enthalpy flows by means of a hypersonic nozzle attached to the end of a free-piston driven shock tube. The hyperboloid is mounted at 15-deg angle of attack within the Mach cone outside the hypersonic nozzle of T3. The leading part of the model sits 150 mm from the nozzle exit during the steady-flow period of each shot (for which the tunnel is completely recoiled a distance of 33 mm). The nozzle is a 7.5-deg half-angle conical nozzle of exit diameter 304.8 mm. It was chosen in preference to the contoured nozzle of the previous work, after findings[12] in relation to contoured nozzles on shock tunnels.

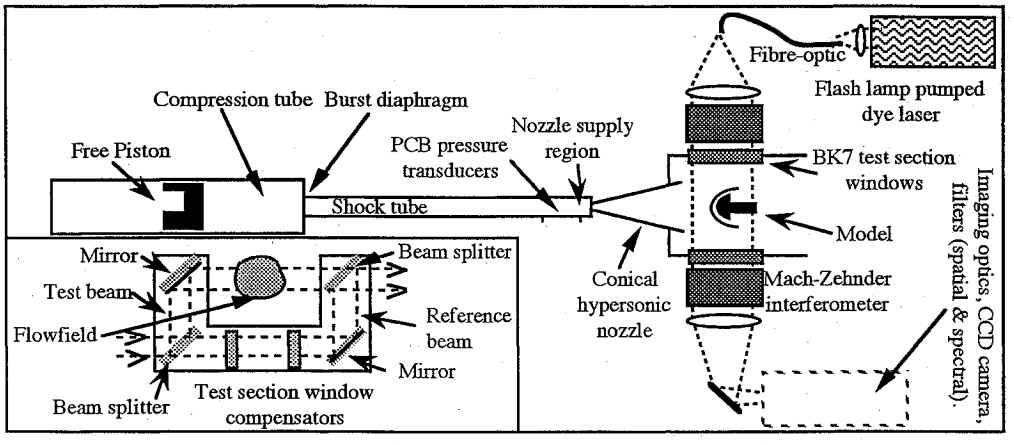

a) b)

Fig. 1 Interferometers: a) Mach–Zehnder interferometer and b) T3 shock tunnel with interferometer.

The model thus sits 1.211 m from the nozzle throat, at a physical area ratio of 183.7, during each shot. Monatomic argon was used as the test gas, with the same operating conditions as in previous work,[2] to provide a low-enthalpy flow that behaves as a perfect gas.

Determination of the Freestream Conditions

The conditions of the flow in the test section were selected by appropriate choices for the partial pressures of argon and helium in the driver gas, the diaphragm rupture pressure, and the shock-tube fill pressure. The pressures and transit times of the primary shock wave were measured with two PCB 113A23 piezoelectric transducers placed 830 and 80 mm from the end of the shock tube. The second transducer also monitored the nozzle supply pressure. Table 1 gives the chosen operating conditions for the tunnel and the measured primary shock velocity. The freestream conditions in the test section at the location of the model were determined as follows. First, the nozzle supply conditions were calculated by well-established shock-tube theory from the measured primary shock speed and nozzle reservoir pressure. Second, the effective nozzle area ratio was determined using measured freestream pitot pressures and an understanding of the nozzle boundary-layer behavior. Third, with a knowledge of the effective nozzle area ratio, the freestream conditions were calculated by theoretical models for inviscid nonequilibrium expansion flows.

For CFD validation purposes, the freestream conditions (including gradients and flow quality) must be known accurately.[1] First, a separate set of experiments at the same operating conditions were run in which a pitot pressure rake (one PCB 113A21 and three PCB 112A21 transducers) was used over several shots to build up pitot pressure profiles across the nozzle exit and across the freestream flow at the location of the model. These profiles, measured at the same postshock reflection delay as the interferometry, are shown in Fig. 2. The test section flow consists of a reasonably uniform core surrounded by the nozzle wall boundary layer. The uniform core displays some structure that is a result in part of the shot-to-shot variations of the tunnel. The overall shape of the structure, however, appears at both locations along the nozzle and probably represents nonuniformities propagating along the flow. For the purposes of determining the freestream conditions, the flow has been assumed to be uniform across the flow, with pitot pressure levels of 211.6 ± 11 kPa at the nozzle exit and 169.8 ± 7 kPa at the location of the nose of the model. The uncertainties quoted are the standard deviations of the pitot pressure measurements and give the spread of pitot pressure assuming it varies across the nozzle.

Using the initial conditions in the shock tube, and the measured shock speed and nozzle supply pressure, the computer program ESTC[13] was used to calculate the conditions behind the reflected shock and then the nozzle supply conditions via an isentropic expansion/compression. ESTC was based on the computer program NENZF.[14] Because of the drainage of the test gas through the nozzle and the wave processes occurring in the nozzle supply region, the nozzle supply pressure exhibits the behavior shown in Fig. 3, where

Table 1 T3 operating conditions

Reservoir pressure	4.51 MPa air
Driver-gas initial pressure	78.9 kPa Ar, 26.7 kPa He
Shock-tube initial pressure	106.4 kPa Ar
Primary shock velocity	1840 ms^{-1}

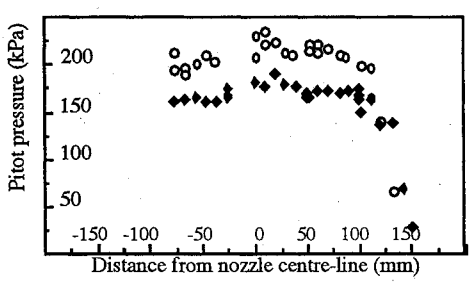

Fig. 2 Pitot pressure profiles across the nozzle flow: ○, nozzle exit and ♦, model location.

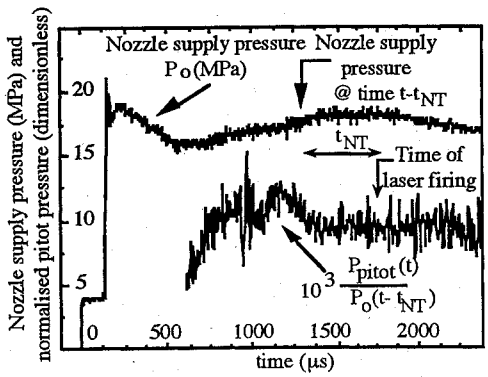

Fig. 3 Nozzle supply pressure and freestream pitot pressure.

drainage is followed by overtailoring. Since the nozzle supply is thus changing with time, knowledge of the time (called here the nozzle transit time t_{NT}) taken for waves to relay a change in nozzle supply pressure to the test section is needed. This time is then subtracted from the time at which the experiment was performed (1750 μs after primary shock reflection) to give the time and conditions in the nozzle supply region appropriate to the experiment. To calculate t_{NT}, the conditions throughout the nozzle and the wave processes within the nozzle supply region must be known. These wave processes affect the pressure measured by the transducer situated 45 mm upstream of the start of the convergence toward the nozzle throat. Their effect will be small, however, because pressure gradients in the nozzle supply region will be much less than in the nozzle itself, and so the nozzle transit time can be represented as $t_{NT} = \int dx/(v + a)$. The integration is performed along the nozzle centerline from the start of the converging section to the location of the model. These parameters are determined by performing a one-dimensional inviscid nozzle calculation with the computer program NENZF and using the true nozzle contour to give the area ratio variation with distance along the nozzle. The nozzle transit time was found to be extremely slowly-varying with changing area ratio, as long as the nozzle length was constant. This effect is because of the compensating effect of a decreasing area ratio for given location causing an increased sound speed but a decreased velocity. An approximation to this nozzle transit time is given by the time difference between the incident shock passing the nozzle supply pressure transducer, propagating through the nozzle, and reaching the model (or pitot pressure rake). The time difference for the present work was $t_s = 440$ μs. Two sets of nozzle supply conditions, calculated with ESTC at times that straddled the approximation given by t_s, were used to calculate limiting values for the nozzle transit time of 440 μs and 463 μs, from which limiting nozzle supply conditions were determined and then averaged. From these average conditions, a final nozzle transit time was calculated as 453 μs, and then final nozzle supply conditions were determined. These conditions were a nozzle supply pressure of 17.4 ± 0.4 MPa, a nozzle supply temperature of 6590 ± 120 K, and a nozzle supply (stagnation) enthalpy of 3.43 ± 0.06 MJkg^{-1}. The variation of nozzle supply pressure with fluctuations in the time at which the interferometry was performed is about ± 0.2 MPa. Shot-to-shot variations are of approximately the same magnitude, whereas variations over a conservative error in the nozzle transit time of ± 50 μs are also ± 0.2 MPa.

The 1750-μs delay (which varied up to 50 μs each way from shot to shot) was chosen to coincide with the plateau of the nozzle supply pressure. Figure 3 also shows the ratio

$$10^3 P_{\text{pitot}}(t)/P_0(t - t_{\text{NT}}) \tag{2}$$

for one of the pitot survey shots, at 50 mm off centerline at the location of the model. Steady flow exists where this ratio is a constant, and commences approximately 1400 μs after the primary shock arrival in the nozzle supply region. Figure 3 shows none of the features associated with a bifurcated reflected shock,[15] which is the primary mechanism thought to be responsible for early test gas contamination by the drivergas.[16] This observation, coupled with the variation of contamination-free test time in T3 for air flows[16] (assuming it

Table 2 Nozzle supply conditions and freestream conditions and gradients

Nozzle supply conditions		Freestream conditions:	Magnitude	Gradient, %
Pressure P_0	17.4 ± 0.4 MPa	Pressure P_∞	$680.8 \pm 8\%$ Pa	−5
Temperature T_0	6590 ± 120 K	Temperature T_∞	$113.6 \pm 1\%$ K	−2
Enthalpy h_0	3.43 ± 0.06 MJkg^{-1}	Velocity v_∞	$2596 \pm 2\%$ ms^{-1}	+0.02
Density ρ_0	12.7 ± 0.3 kgm^{-3}	Density ρ_∞	$0.02880 \pm 7\%$ kgm^{-3}	−3
Nozzle transit time	453 μs	Mach number M_∞	$13.06 \pm 2\%$	+1

is applicable to argon flows and extrapolating it to the present low enthalpy), indicates that driver-gas contamination occurs well after the 1750-μs time. Thus, the current work utilized steady flow, but was done not too long after steady flow onset to avoid the problem of driver-gas contamination.

With knowledge of the nozzle supply conditions, the nozzle flow can be calculated using the two-dimensional inviscid nonequilibrium chemistry program SURF.[17] At first the true nozzle contour is used, and then the area ratios that give the measured pitot pressures are used to determine an effective nozzle angle that accounts for the nozzle boundary layer. SURF is then run again using this angle, and the calculated conditions at the location of the model are used as the freestream conditions for the CFD code.

To confirm the present use of this method of accounting for the nozzle wall boundary layer, an alternative method was also used as follows. Edenfield[18] determined, from measurements from various hypersonic wind tunnels, a displacement thickness δ^* correlation given by

$$\delta^*/x = 0.42(Re_{\text{ref}})^{-0.2775} \tag{3}$$

where Re_{ref} is the reference Reynolds number:

$$Re_{\text{ref}} = \rho_{\text{ref}} \cdot v_\infty \cdot x/\mu_{\text{ref}} \tag{4}$$

Here v_∞ is the freestream velocity at x; ρ_{ref} and μ_{ref} are the density and viscosity evaluated at the freestream pressure p_∞ and Eckert's reference enthalpy[19]

$$h_{\text{ref}} = 0.5(h_w + h_\infty) + 0.22r(h_{\text{stg}} - h_\infty) \tag{5}$$

For a turbulent boundary layer, r (the recovery factor) $= (Pr)^{1/3}$.

This correlation was applied as follows. SURF was used to calculate the conditions at the exit of the nozzle as a function of nozzle angle. The correlation was used to determine the displacement thickness there for each angle. A geometrical displacement thickness can be defined as the true nozzle exit radius (152.4 mm) minus the effective radius for each angle. As the angle is decreased from its true value, the Edenfield displacement thickness also decreases, whereas the geometrical displacement thickness sharply rises. The angle for which the two values for displacement thickness agree is the nozzle angle that is consistent with the Edenfield boundary-layer correlation as applied to the present physical nozzle. This angle was 6.60 deg (nozzle half-angle), for which SURF determined the pitot pressures at the nozzle exit and model location to be 217.7 and 171.4 kPa, respectively, which agree with the experimental values. Hence, the experimental pitot pressure results used here to account for the nozzle-wall boundary layer are in agreement with results from other facilities. The effective area ratio at the model tip is, thus, $A/A^* = 145$.

The freestream values and gradients at the location of the model are given, along with the nozzle supply values, in Table 2. The key values that affect this work are Mach number = 13.06 and density = 0.0288 kgm^{-3}. They change by +1 and −3%, respectively, in the direction of streamlines, over the region analyzed in this work, because of the conicity of the flow. The maximum freestream angular deflection from the nozzle centerline over the region presented is 0.7 deg. Thus, the effects of axial- and radial-flow gradients, because of the use of a conical nozzle, can be ignored. The freestream uncertainties quoted were calculated by applying the variations in nozzle reservoir conditions and measured freestream pitot pressure to the nozzle flow calculation. This gives the possible variation of Mach number and density across the freestream that will affect the shock-layer density field and, hence, the experimental phase maps. The small uncertainties quoted for the temperature and velocity represent the variation of those quantities when tied by perfect-gas laws to the varying pressure and density.

Interferometry

To probe the density distribution in the shock layer, a Carl Zeiss Mach–Zehnder interferometer was used to produce finite fringe interferograms of the flowfield and freestream, as shown in Fig. 1. The light source used was a homemade grating tuned flash lamp pumped dye laser operating with the laser dye Rhodamine 6G. After narrowband spectral filtering, the wavelength λ was 589.1 nm (full width at half-maximum = 0.6 nm). Spatial filtering was also used in the collection optics, with both forms of filtering serving the purpose of eliminating the luminosity associated with flow impurities being excited by the high temperatures in the shock layer. With fringes focused at the plane of the model, the interferogram was imaged onto a charge-coupled device camera such that one dimension of the camera, parallel to the freestream, caught approximately 30 mm of the model and 25 mm of the freestream. This was sufficient to resolve 18 pixels between the model and the bow shock at the stagnation streamline. Two interferograms were taken for each shot: a reference interferogram just prior to the shot and a test interferogram during the shot. Each digitized interferogram was stored on a personal computer for later processing into phase shift maps.

The personal computer also controlled the firing of the laser. This was done after the preset 1750-μs delay had elapsed after arrival of a trigger signal from the primary shock passing the nozzle supply region pressure transducer.

To compare the predictions of the CFD code with the experimental data, theoretical phase maps are computed by applying the interferometer equation[8] along lines of sight through the flowfield. This equation for a monatomic gas relates the total phase shift ϕ of light, with wavelength λ, propagating along each line of sight, to the density ρ of the fluid at each point:

$$\phi = 2\pi K/\lambda \int \rho \, ds \tag{6}$$

The integration is along the line of sight. For the present work, $\lambda = 589.1$ nm, for which $K = 1.58 \times 10^{-4}$ m^{3}kg^{-1} (interpolated from the data presented by Leonard[20]). A Cartesian coordinate system $\boldsymbol{u}, \boldsymbol{v}, \boldsymbol{w}$ is set up such that $\boldsymbol{u}$ lies along the direction of the freestream flow and $\boldsymbol{v}$ lies along the line of sight across the flowfield. Integration is performed along each $\boldsymbol{v}$ ray (which are spaced by the pixel dimensions in the experimental data), with the integrated phase shift forming a map in the $\boldsymbol{u}, \boldsymbol{w}$ plane. The limits of integration are the same for each ray and lie outside the shock layer. The phase shift ϕ_∞ that would exist in the absence of the model is subtracted from ϕ to yield the phase shift because of the blunt body flow only.

An interpolation from the curvilinear body-centered coordinate system of the CFD code to the Cartesian system of the phase integration is performed to give the density at each point along each ray. To avoid time consuming grid searches to achieve this, the analytical shape of the model is used to determine in which curvilinear grid cell each point on the line of sight lies. The interpolation is then done in computational (grid indices) space rather than with the distorted physical grid, ensuring that no discontinuities are produced within the shock layer.

As was discussed earlier, seven different viewing angles θ (in 15-deg increments from the θ = 0-deg position where the model, at attack, is side-on to the optical axis) were employed to remove the ambiguity associated with the measurement of an integrated flow parameter. This was achieved by rotating the central sting holding the model between shots.

Image Processing

The raw interferograms contain phase information not only for the flowfield being investigated, but also from sources such as the spatial profile of the laser, imperfections in the optics, background luminosity (admittedly minimized here by the filtering employed), and random noise. To extract the flowfield phase information from each interferogram, the semiautomated two-dimensional Fourier transform fringe analysis software FrAnSys[21] was used.

The two-dimensional Fourier transform technique makes use of the separation in the Fourier transform plane of many of the contributions to the interferograms intensity distribution, because of the heterodyning process (the production of finite fringes by tilting an interferometer component). By filtering out all other components in the transform plane, the component containing the flowfield information can be selected and retransformed to give modulo 2π of the phase. The true phase is recovered using an unwrapping technique.[22] To remove the heterodyning and optics contributions, we subtract a similar result gained from a no-flow interferogram.

This is only a first approximation; however, the subtracting of the two results relies on the alignment of the two interferograms, and any rotational misalignment will be manifested as a linear component of the phase distribution. There is also the possibility of slight changes occurring to the heterodyning between the recording of each interferogram. For a more accurate result, a region that is known to be undisturbed by the flow is chosen from the first approximation to the phase distribution. In the present work, the freestream region is used. The method of least squares is used to fit a plane to the phase shift in this region, and this plane is then extrapolated and subtracted from the entire image, removing the linear background and accounting for the possible changes to the heterodyning mentioned. In the current work, the region upstream of the shock was chosen, and assumed to have negligible variation of phase shift, since (as already stated) the freestream flow gradients are small and the variation of path length through the test core is also negligible across the small size of the region of interest. The result of the subtraction is the phase shift because of the shock layer only, giving a mean value of zero across the phase distribution outside the shock layer. This subtraction procedure corresponds to the procedure described for generating the theoretical phase maps. After performing this subtraction, however, a one-dimensional (normal to the freestream direction) modulation of the phase remained, suggestive of inhomogeneities across the nozzle propagating downstream. This was dealt with as follows. The freestream part of the region bordered by two lines of constant u touching the model tip and one or two pixels upstream of the shock vertex, respectively, was averaged in the streamwise direction to give an average cross section of the modulation. This was then subtracted from each cross section of constant u in the entire image, leaving the freestream for cross sections between the shock and model free of all modulation except high-frequency noise.

In the two-dimensional Fourier transform, the image is assumed to be one period of a continuous infinite cycle. To avoid the problem of discontinuities at the boundary of the image (and at the edge of the model) causing streaking of information across the Fourier plane, FrAnSys enlarges the image by adding a strip of zeros outside each border, and iteratively extends the fringes into the new region and into the model so that they vary continuously across each boundary. This is done by transforming the extended data; retransforming a small region around the heterodyning frequency and the origin; merging the original data back in; and iterating, with gradually increasing filter size, until a smooth fringe extension is achieved.

Results

Using the methods described, experimental phase maps were produced from which the various nonflow phase contributions (except for some random noise) have been removed. In addition, phase maps, with freestream phase subtracted, were computed from the inviscid solution by the CFD method for the present conditions. As stated earlier, the boundary layer has negligible effect on the structure of the inviscid shock layer at these conditions, and so phase maps for an uncoupled (inviscid only) solution are presented. From computed boundary-layer thicknesses, the viscous flow region would occupy at most a two pixel thick layer next to the body in the region analyzed.

Figure 4 is a digitized interferogram for a shot with viewing angle θ equal to 60 deg. The dimensions of each unextended image are 320×100 pixels, with each pixel representing 0.145 ± 0.001 mm horizontally and 0.215 ± 0.001 mm vertically. The direction of the freestream flow is along the vertical u direction, and the stagnation point lies at the middle of the image. The fringe shift at the bow shock, as well as various chips (because of diaphragm fragment hits) on the test section windows, can be clearly seen. The interferogram shown does not include the fringe extension. Lines depicting the location of cross sections shown later are drawn and labeled. Figures 5a and 5b show 20-color gray-scale images for both experimental and theoretical phase maps for the two extremes of the seven viewing angles used ($\theta = 0$ and 90 deg). The comparison between the theoretical and experimental phase maps is extremely good, given the noise present in the experimental maps, for both cases. The experimental phase is slightly higher than the theoretical phase for the windward side for $\theta = 0$. This is discussed later. Some noise can be seen in the freestream region of Figs. 5a(a) and 5b(a). In general, for each θ, fluctuations across the experimental phase maps are less than 5% of the maximum phase shift in each case. Another feature of Figs. 5a and 5b is the good agreement between the experimental and theoretical shock shapes.

It is appropriate at this point to describe the uncertainties in the comparisons because of positioning errors: uncertainties in the calibration of the scale of the experimental interferograms have led to slight scale differences between the theoretical and experimental images; the uncertainty in the stagnation-point determination for the model from the interferograms has led to slight translational uncertainties between the images; and uncertainty in the original viewing angle (±2 deg) has led to slight shape differences between experimental and theoretical body outlines. Overlaying these body outlines has shown that overall, there is possibly a 1–2 pixel uncertainty in any direction when comparing experimental and theoretical phase shifts at any point. The stagnation-streamline shock-standoff comparison shows at most a 1–2 pixel discrepancy (~5–10% of the standoff distance) in each case.

Figures 6a–6c show the phase shift profiles for the cross sections of constant u shown in Fig. 4, for the phase maps for $\theta = 0, 45$, and 90 deg, respectively. Two theoretical profiles (dark lines) are shown with each experimental slice (faint lines), representing in Figs. 6a and 6c the upper and lower limits of the freestream density ($\rho_\infty \pm \Delta\rho_\infty$) and in Fig. 6b profiles (for ρ_∞) for slices adjacent to the experimental profiles. Figures 7a–7c present phase shift profiles for each case represented in Fig. 6, except that the slices of constant w of Fig. 4 are used.

For $\theta = 0$ deg, the departure from axial symmetry is very pronounced. Of particular note are slices 75 (u = const) and 60 and 260 (w = const), for which the experimental results show a slightly larger departure from symmetry than the theoretical results. Three possible explanations for this discrepancy between theory and experiment are considered here: the CFD code is in error and is underpredicting the density of the shock standoff distance in this region of the flow; in the experiment, the freestream flow is nonuniform with a higher density and lower Mach number flow incident on the windward surface; or pixel misalignment is causing slightly different slices to be compared. Figure 2 indicated variations in the pitot pressure and, therefore, the Mach number and density across the freestream. At the hypersonic Mach numbers generated by the T3 shock tunnel, the shock-standoff distance for near-normal shock waves will not be sensitively dependent on Mach number variations.

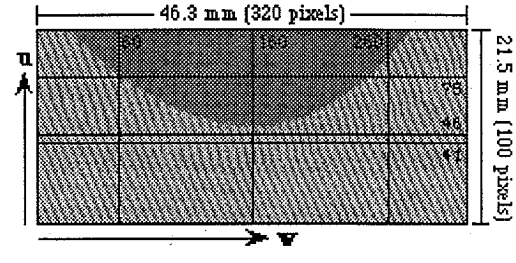

Fig. 4 Interferogram for θ = 60 deg (not extended); numbered lines represent profile locations for Figs. 7 and 8.

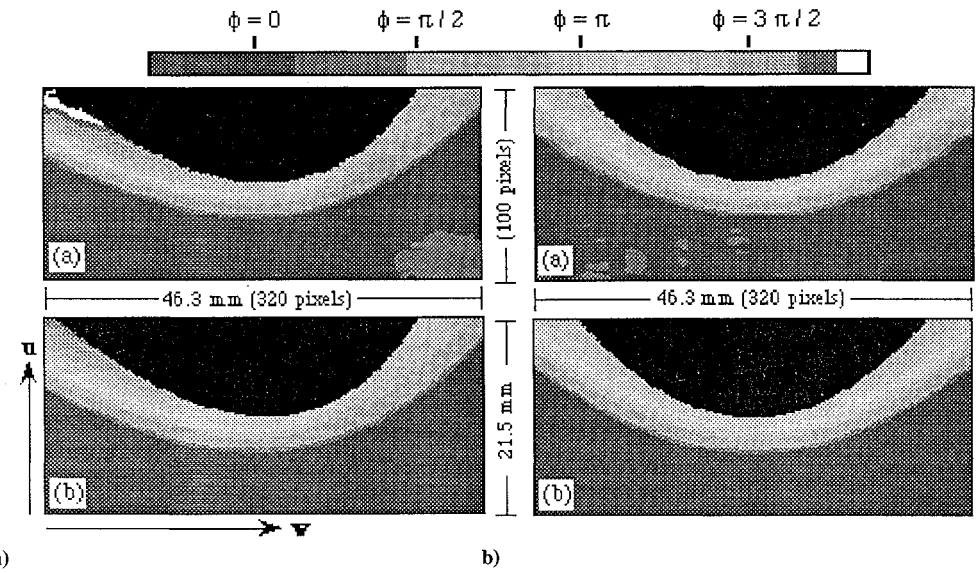

Fig. 5 Phase maps for a) $\theta = 0$ deg and b) $\theta = 90$ deg [(a) experiment and (b) theory].

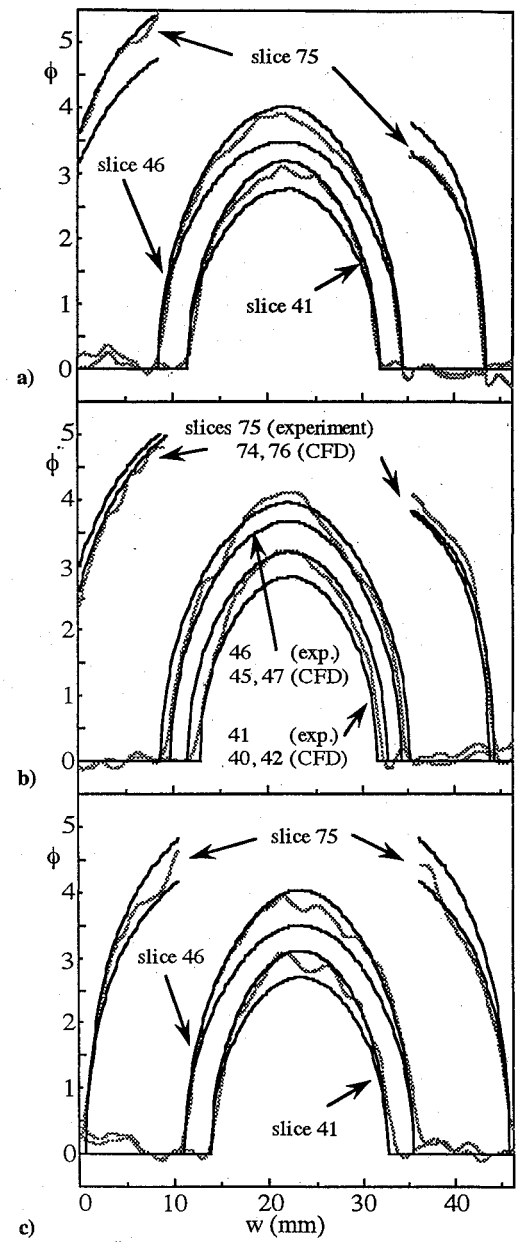

Fig. 6 Phase shift profiles along slices with constant u: a) $\theta = 0$, b) $\theta = 45$, and c) $\theta = 90$ deg.

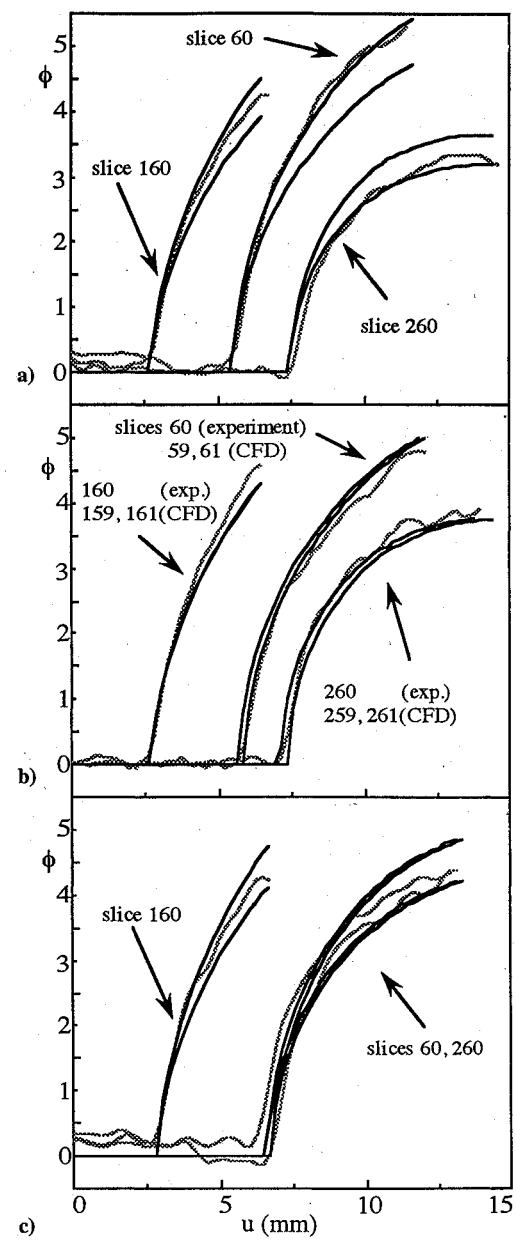

Fig. 7 Phase shift profiles along slices with constant w: a) $\theta = 0$, b) $\theta = 45$, and c) $\theta = 90$ deg.

Density variations in the freestream, however, will cause density variations and, hence, integrated phase shift variations, in the shock layer. Figures 6a and 7a indicate that a variation of $2\Delta\rho_\infty$ in density between the flow incident upon the windward and leeward surfaces would be sufficient to account for the observed discrepancy. Figures 6b and 7b show only a small variation between theoretical slices away from the nose for $\theta = 45$ deg, and this result also holds for $\theta = 0$ deg, suggesting that pixel misalignment is not the cause for the discrepancy. As Figs. 6 and 7 show, the theoretical and experimental shock-standoff distances agree well, and so this is not the cause for the discrepancy. The most likely cause is nonuniformities in the freestream flow. The effect of the bowshock will be to magnify any such nonuniformities, and it is possible, therefore, that the background subtraction technique used has to a large extent removed the effect of such nonuniformities from the freestream phase shift, but only to a small extent from the shock layer. If the modulations that were removed are indeed integrated downstream-propagating nonuniformities, then tomographic reconstruction could be used to quantify them.

The comparisons presented in Figs. 6 and 7 indicate that for each viewing angle, the theoretical phase shift agrees well with the experimental phase shift to within experimental error, which has a phase measurement component (from the fluctuations because of noise and from misalignment between images) and a freestream uncertainty component (particularly the density). This also applies to the four viewing angles not presented.

Some caution must be used with regard to the use of integrated quantities such as phase shift in attempting to validate CFD codes. Good agreement between a code and experimental data in an integrated measurement domain such as the phase shift distribution does not imply that the agreement back in the fluid dynamic domain will be as good. Two concerns[8] are 1) that the integrated quantities for any flowfield are not unique to that flowfield and 2) that differences between theory and experiment in the measurement domain are not linearly related to differences in the fluid domain. The first concern has been addressed in the present work by using multiple viewing angles, and although a large number of angles would be required to totally eliminate this concern, the good comparisons for the seven angles available minimizes it. The second concern is highlighted by the fact that tomographic reconstruction of accurate projections of a theoretical object differ significantly from reconstructions using the same projections with noise added.[23] In other words, validation to a certain level of precision of theoretical integrated quantities using measured integrated quantities does not necessarily imply that the original theoretical flowfield is validated to the same level. The fact that the comparisons shown are very good, however, is a necessary (despite not being sufficient) condition for agreement between the actual theoretical and experimental flowfields, and as such provides confidence in the validity of the density calculation of the three-dimensional inviscid CFD code.

Conclusions

This study has provided a valuable comparison between experimentally measured and theoretically calculated flowfields. By obtaining interferometric projections for a large number of lines of sight, it has been possible to study a nonaxially symmetric shock-layer flowfield. The theoretically predicted phase maps and shock shapes compare well with the experimental results. Discrepancies that do exist between theory and experiment are explainable in terms of measurement uncertainty and nonuniformities in the freestream. This work has completed an important preliminary step required before the implementation of tomographic reconstruction methods. Furthermore, the results obtained will provide a valuable database for the tomographic reconstruction work. Finally, these experiments with a perfect-gas flow provide confidence in the validity of the CFD code and are an important initial step in the code validation process for the more general case of nonequilibrium real-gas flows.

Acknowledgments

This work was financially assisted by the Sir Ross and Keith Smith Fund, NASA Grant NAGW 1467, and the Australian Research Council. The CFD code was developed and made available by Deutsche Aerospace. The authors also gratefully acknowledge the skillful technical support and operation of the T3 Shock Tunnel by Paul Walsh in the experimental work.

References

[1]Chapman, G. T., "An Overview of Hypersonic Aero-Thermodynamics," *Communications in Applied Numerical Methods*, Vol. 4, No. 3, 1988, pp. 319–325.

[2]Boyce, R. R., and Mundt, C., "Aerodynamical CFD Studies of Re-Entry Flows," *Proceedings of the International Aerospace Congress 1991*, Vol. 3, Inst. of Engineers, Canberra, Australia, 1991, pp. 23–31.

[3]Boyce, R. R., and Mundt, C., "Computational Fluid Dynamics Code Validation Using a Free-Piston Hypervelocity Shock Tunnel," *Shock Waves: Proceedings of the 18th International Symposium on Shock Waves* (Sendai, Japan), edited by K. Takayama, Vol. 2, Springer–Verlag, Berlin, 1991, pp. 1127–1132.

[4]Boyce, R. R., Pulford, D. R. N., Houwing, A. F. P., Mundt, C., and Sanderman, R. J., "Comparisons of Nonequilibrium Chemistry CFD Calculations with Broadband CARS Measurements of Local Temperatures in Hypervelocity Nitrogen Blunt Body Flows," *Shock Waves at Marseilles: Proceedings of the 19th International Symposium on Shock Waves* (Marseilles, France), edited by R. Brun and L. Dumitrescu, Vol. 2, Springer–Verlag, Berlin, 1995, pp. 235–240.

[5]Sutton, D. J., Houwing, A. F. P., Palma, P. C., Boyce, R. R., and Sandeman, R. J., "The Application of Laser Induced Predissociation Fluorescence to the Measurement of Vibrational Temperatures in a Shock Layer Flow," AIAA Paper 93-3071, July 1993.

[6]Hornung, H. G., "Nonequilibrium Dissociating Flow over Spheres and Circular Cylinders," *Journal of Fluid Mechanics*, Vol. 53, Pt. 1, 1972, pp. 149–176.

[7]Park, C., and Yoon, S., "Fully Coupled Implicit Method for Thermo-Chemical Nonequilibrium Air at Suborbital Flight Speeds," *Journal of Spacecraft and Rockets*, Vol. 28, No. 1, 1991, pp. 31–39.

[8]Merzkirch, W., *Flow Visualization*, 2nd ed., Academic, Orlando, FL, 1987, p. 119.

[9]Monnoyer, F., Mundt, C., and Pfitzner, M., "Calculation of the Hypersonic Viscous Flow Past Reentry Vehicles with an Euler-Boundary-Layer Coupling Method," AIAA Paper 90-0417, Jan. 1990.

[10]Mundt, C., "Calculation of Hypersonic, Viscous, Non-equilibrium Flows around Reentry Bodies Using a Coupled Boundary-Layer/Euler Method," AIAA Paper 92-2856, July 1992.

[11]Stalker, R. J., "Development of a Hypervelocity Wind Tunnel," *Aeronautical Journal of the Royal Aeronautical Society*, Vol. 76, June 1972, pp. 374–384.

[12]Gai, S. L., "Free Piston Shock Tunnels: Developments and Capabilities," *Progress in Aerospace Science*, Vol. 29, 1992, pp. 1–41.

[13]McIntosh, M. K., "Computer Program for the Numerical Calculation of Frozen and Equilibrium Conditions in Shock Tunnels," Dept. of Physics, Australian National Univ., ANU Internal Rept., Canberra, Australia, Sept. 1968.

[14]Lordi, J. A., Mates, R. E., and Moselle, J. R., "Computer Program for the Numerical Solution of Nonequilibrium Expansions of Reacting Gas Mixtures," NASA CR-472, 1966.

[15]Sanderson, R. J., "Interpretation of Pressure Measurements Behind the Reflected Shock in a Rectangular Shock Tube," *AIAA Journal*, Vol. 7, No. 7, 1969, pp. 1370–1372.

[16]Stalker, R. J., and Crane, K. C. A., "Driver-Gas Contamination in a High-Enthalpy Reflected Shock Tunnel," *AIAA Journal*, Vol. 16, No. 3, 1978, pp. 277–279.

[17]Rein, M., "SURF: A Program for Calculating Inviscid Supersonic Reacting Flows in Nozzles," Graduate Aeronautical Labs., California Inst. of Technology, GALCIT FM 89-1, Pasadena, CA, Nov. 1989.

[18]Edenfield, E. E., "Design of a High Reynolds Number Mach Number 8 Contoured Nozzle for the Hypervelocity Wind Tunnel (F)," Arnold Engineering Development Center, AEDC-TR-72-48, Arnold AFB, TN, Aug. 1972.

[19]Eckert, E. R. G., "Engineering Relations for Friction and Heat Transfer to Surfaces in High Velocity Flow," *Journal of Aeronautical Sciences*, Vol. 22, No. 8, 1955, pp. 585–587.

[20]Leonard, P. J., "Refractive Indices, Verdet Constants and Polarizabilities of the Inert Gases," *Atomic and Nuclear Data Tables*, Vol. 14, No. 1, 1974, pp. 21–37.

[21]Bone, D. J., "A Users Guide to FrAnSys—a Fringe Analysis System from Australian National University," Dept. of Physics, Australian National Univ., ANU Internal Rept., Canberra, Australia, Sept. 1991.

[22]Bone, D. J., "Fourier Fringe Analysis: the 2-D Phase Unwrapping Problem," *Applied Optics*, Vol. 30, No. 25, 1991, pp. 3627–3632.

[23]Morton, J. W., "Tomographic Imaging of Supersonic Flows," Ph.D. Thesis, Dept. of Physics, Australian National Univ., Canberra, Australia, Nov. 1995.

I. D. Boyd
Associate Editor